Investigation of a Separated Nozzle Flow with Transonic Resonance Using Dynamic Mode Decomposition

Chalmers Research Report 2014:04

ISSN 1652-8549

Ragnar Lárusson,* Niklas Andersson † and Lars-Erik Eriksson ‡
Chalmers University of Technology, SE-41296 Gothenburg, Sweden.

Jan Östlund §
GKN Aerospace Sweden AB, SE-46181 Trollhättan, Sweden.

1 Introduction

Transonic tones in convergent-divergent nozzles have received an increased attention in recent years. These tones, which result from a resonance phenomenon associated with a shock inside of the divergent part of the nozzle, are interesting as a flow phenomenon in itself and from a engineering viewpoint since resonance is always a concern in the design of high speed flow devices. Zaman et al.[1] investigated transonic tones in a convergent-divergent axisymmetric nozzles experimentally. The resonance frequencies where obtained through spectral analysis of microphone data. The results showed an increase in frequency with increasing nozzle pressure ratio with a staging behavior where high frequency odd harmonic stage resonates at lower pressure ratios and a lower frequency fundamental stage resonates at higher pressure ratios. It was further concluded that the resonance mechanism involved either a standing 1/4 wave or a 3/4 wave between the shock and the nozzle exit depending on at which stage the resonance took place. For the pressure fluctuations, this would result in a wave node near the nozzle exit and a antinode just downstream of the shock. The results further showed that the resonance frequency, within a stage, inversely scales with the distance from the foot of the separation shock to the nozzle exit. Ching and Zaman [2] carried out a numerical investigation of the phenomenon and showed that the resonance frequencies could be predicted with reasonable accuracy from an axisymmetric simulation.
Large Eddy Simulations by Olson and Lele [4] of a separated flow inside a planar-nozzle confirmed that the frequency of transonic resonance is dependent on the distance from the shock to the nozzle exit. They also suggest that there exists a feedback loop between the separated shear layer and the shock. In this feedback loop, information travels downstream from the boundary layer shock interaction region and is convected through the shear layer while a pressure wave travels upstream through the subsonic region downstream of the shock.
In the present study the Dynamic Mode Decomposition (DMD) algorithm, proposed by Schmid [3], was applied to the same nozzle investigated in Ref.[2] and Ref.[1] in order to find out if the algorithm, when applied to a perturbed URANS flow simulation, is capable of predicting transonic resonance frequency. The DMD uses a set of observation data from a nonlinear flow simulation, and performs a modal decomposition under the assumption that the flow dynamics represented in the data are linear, see Schmid [3]. The observation data, in this case, consisted of snapshots from a 2D axisymmetric

*PhD Student, Department of Applied Mechanics, Chalmers University of Technology, Sweden.
†Assistant Professor, Department of Applied Mechanics, Chalmers University of Technology, Sweden.
‡Professor, Department of Applied Mechanics, Chalmers University of Technology, Sweden.
§Method specialist, Department of Aerothermodynamics, GKN Aerospace Sweden AB.

URANS simulation of the perturbed nozzle flow. The DMD algorithm employs the singular value decomposition (SVD) to form an orthogonal projection base to build a system matrix of reduced size, which can be subjected to direct eigendecomposition. Some of the eigenmodes of the reduced system will then be good approximations of the eigenmodes of the full system.
Results for two different nozzle pressure ratios are presented. In both cases, modes with frequencies close to what was observed in the experiments by Zaman et al.[1] were detected. These modes were either growing or had a relatively small damping compared with other modes detected in the DMD. Furthermore, higher harmonic modes were found as well. Analyses of the temporal behavior of these modes show a standing pressure wave between the shock and the nozzle exit.

2 Method and Case

2.1 Geometry and Computational Mesh

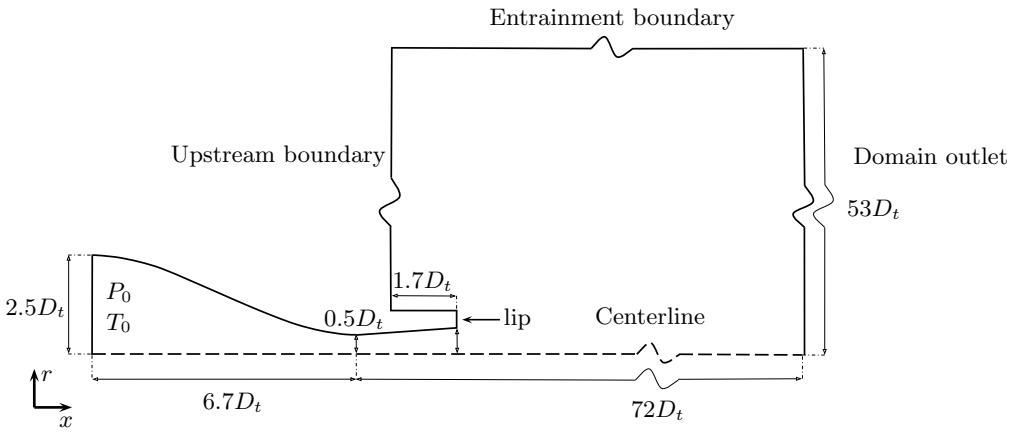

Figure 1: Schematic representation of nozzle geometry and computational domain.

Figures 1 and 2 show the geometry of the nozzle and the computational mesh respectively. The throat diameter of the nozzle is $D_t = 0.00762$ m. Other dimensions in terms of throat diameter are: inlet diameter $D_{in} = 5.0D_t$, outlet diameter $D_{out} = 1.33D_t$. The area ratio between the exit and the throat is 1.77. The distance from the throat to the exit is $L = 2.5D_t$. The thickness of the nozzle lip is $0.44D_t$.

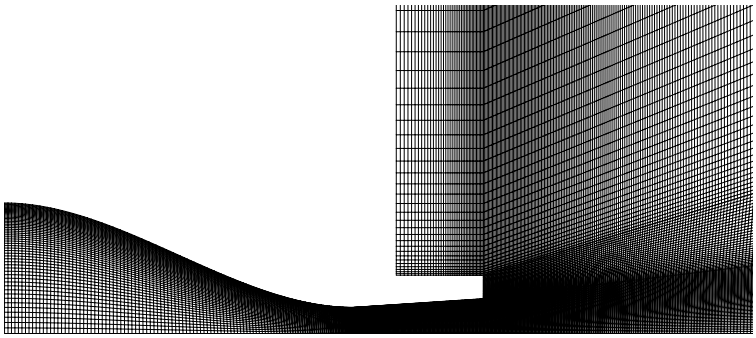

Figure 2: The computational mesh showing the geometry of the nozzle.

The computational mesh used is two-dimensional, block-structured and non-orthogonal. The mesh

consists of 9 blocks and roughly 66,000 cells. The bulk of the cells are located within the nozzle and in the immediate surroundings downstream of the nozzle exit as seen in Figure 2. The computational domain extends approximately $72D_t$ and $53D_t$ from the throat in the axial and radial directions respectively as indicated in Figure 1.

2.2 Boundary Conditions and Mean Flow

Boundary conditions for the RANS/URANS simulations were as follows; On the centerline axis, singularity conditions were applied. At the domain exit a static pressure P_a was prescribed. Absorbing boundary conditions based on the method of characteristics were applied on the nozzle inlet boundary and the entrainment and upstream boundaries of the domain.
At the inlet, density, axial velocity and, pressure were prescribed calculated from a given inlet total pressure, P_0, total temperature, T_0 and inlet to throat are ratio, using isentropic flow equations. A total temperature of $298K$ was constant over the whole domain and the ambient pressure was $P_a = 99284.505$ Pa in both cases. The simulations were carried out using the code volsol++, jointly developed at GKN Aerospace Sweden AB and Chalmers University of Technology.

2.3 Cases

Two cases of different nozzle pressure ratios were investigated in the present study. Figure 3 a) and b) show the Mach number distribution for Case I and Case II, respectively. These flow solutions, acquired from a steady state RANS simulation, were used as reference states in the DMD algorithm, which is explained in section 2.4.
Case I, which had a pressure ratio of $P_0/P_a = 1.42$, featured a restricted shock separation (RSS) in which the separated flow reattached to the wall, forming a close circulation bubble downstream of the shock. Case II had a higher pressure ratio of $P_0/P_a = 2.39$ and a free shock separation (FSS) where the separated flow did not reattach to the wall and the recirculation zone extended all the way to the exit of the nozzle, forming an "open" separation bubble. This formed a "lambda foot" shock and a shock cell pattern, or a shock train, downstream of the separation. For further reading on nozzle flow separation the reader is referred to Ref. [5].
As mentioned above, Zaman et al. [1] reported a staging behavior of the tone frequency as the nozzle inlet pressure was increased. This was registered as a sudden change of the transonic tone from a high frequency to a lower frequency. This jump corresponded roughly to a jump from a third harmonic frequency to a fundamental frequency (first harmonic). In Ref. [1] it is suggested that this shift occurs when the flow transitions from a restricted flow separation with a relatively small separation bubble, as in Case I, to a "lambda foot" shock pattern with a separation bubble of size comparable with the distance from the separation to the nozzle exit, as in Case II, see Figure 3 b). It was further concluded in Ref. [1] that there seemed to be, on a time-average scale, a closed separation bubble in both cases. They do not show, however, any evidence explicitly showing that it is in fact so for the lower frequency resonance stage. There is therefore no strong reason to doubt that the FSS separation observed in the RANS solution presented here is a false prediction of the flow field.

2.3.1 On Separation Location

The contour of the divergent part of the nozzle has a conical form with a relatively low divergence angle. As a consequence, a small change in the inlet pressure results in a relatively large shift in the separation location. This characteristic makes it difficult to predict the separation correctly in the RANS simulation. Both a realizable k - ε and the Menter-SST turbulence models failed to predict the location very accurately. The realizable k - ε model was chosen since it uses wall functions and therefore does not need to have the boundary layer resolved as the Menter-SST model does.
Another intriguing phenomenon observed in Ref. [1] is worth mentioning: The separation location for a number of different operating points was recorded and an interesting behavior was noticed; For low nozzle pressure ratios the point of separation moves downstream with increased pressure ratio. At a certain point the separation location moves back upstream and then proceeds to move downstream

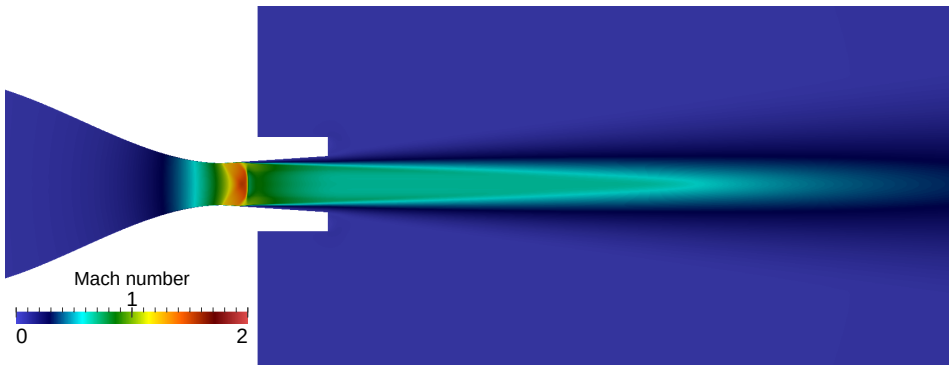

(a) Case I, $P_0/P_a = 1.42$

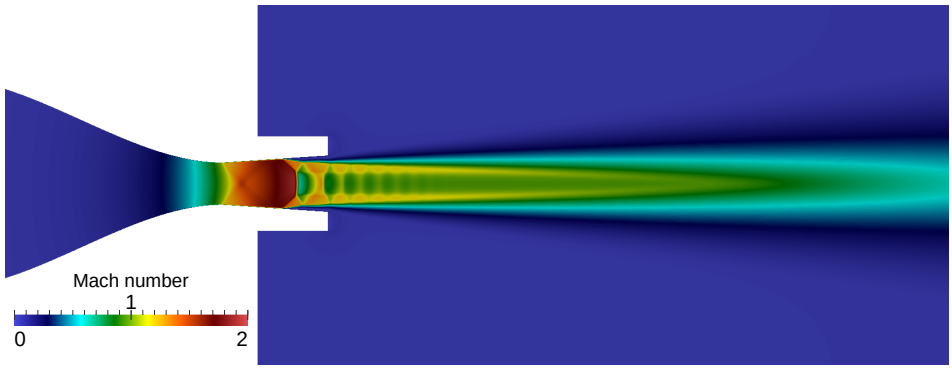

(b) Case II, $P_0/P_a = 2.39$

Figure 3: Mach number distribution in the reference flow states.

with increasing pressure ratio but at an increased rate (this can be seen in Figure 16 in [1]). This is probably linked to the abovementioned transition from RSS flow to a FSS flow. A similar and more common shift in separation location is observed in nozzles where the flow switches first from FSS to RSS as the inlet pressure increases, causing the separation location to jump downstream [5]. Given this information, it becomes relevant to compare our mode frequencies with experimentally observed frequencies both with respect to nozzle pressure ratio and separation location.

2.4 Dynamic Mode Decomposition

The DMD algorithm used in the current study is the SVD variant proposed by Schmid[3]. A given set of flow field snapshots, $\{q_0, ..., q_m\}$ sampled at a fixed rate, are organized into a data matrix

$$Q_0^{m-1} = \{q_0, q_1, ..., q_{m-1}\}, \tag{1}$$

for discrete time steps k = 0 to k = $m-1$ and,

$$Q_1^{m} = \{q_1, q_2, ..., q_{m}\}, \tag{2}$$

for discrete time steps k = 1 to k = m. Each snapshot, say of size n, can contain all or some of the flow properties in all or some of the computational grid cells. It is easy to show that if we assume that the linear operator B applies to this data such that $Bq_k = q_{k+1}$ then

$$BQ_0^{m-1} = Q_1^{m}. \tag{3}$$

The data matrix Q_0^{m-1} is factorized using the Singular Value Decomposition (SVD) according to

$$Q_0^{m-1} = U\Sigma W^T, \tag{4}$$

where U is a n x m orthogonal matrix whose columns are referred to as the left singular vectors of Q_0^{m-1}. W^T is a m x n orthogonal matrix whose rows are referred to as the right singular vectors of Q_0^{m-1}. Σ is a m x m diagonal matrix containing the singular values of Q_0^{m-1}. The singular values, σ_i are ordered in such a way that the largest singular value is placed on the first diagonal element and smallest on the last diagonal element, that is $\sigma_0 > \sigma_1 > ... > \sigma_{N-1}$. The projection of B on to the subspace spanned by the left singular vectors can now be written as follows:

$$U^T B U = U^T Q_1^m W \Sigma^{-1} = S_m. \tag{5}$$

S_m is now a reduced matrix of size m x m and can be subjected to direct eigendecomposition to solve $S_m y_i = \mu_i y_i$ where μ_i and y_i are the i^{th} eigenvalue and eigenvector of S_m respectively. We then define the i^{th} DMD mode of B, ϕ_i, as

$$\phi_i = U y_i. \tag{6}$$

In practice, some of the eigenvalues of S_m converge to the eigenvalues of B.

The DMD modes are scaled so that they fulfill

$$q_k = \sum_{i=0}^{m} \mu_i^k \phi_i \qquad , k = 0, ..., m. \tag{7}$$

The norm of the modes can thus give an indication of how much each mode contributes to each snapshot. The eigenvalues, μ, are decomposed in to a real and an imaginary part according to $\mu = \xi + i\omega$. The real part, ξ, represent the damping or growth of the eigenmode and the imaginary part, $\omega = 2\pi f$, represents the temporal fluctuation with frequency f. The relationship between μ, the damping factor ξ, and frequency f is

$$Arg(\mu) = 2\pi f \Delta t + 2\pi b \ , \tag{8}$$

$$\xi = \frac{\ln(Abs(\mu))}{\Delta t} \ , \tag{9}$$

where b is an unknown integer. To determine the value of the integer b, additional work is required such as measuring the wavelength of acoustic waves which could be visible in the flow field of the corresponding mode.

Note that the temporal evolution of a mode ϕ_k can be computed according to

$$\Re(\phi_k e^{\omega t} e^{\xi t}) = \left[\Re(\phi_k)\cos(\omega t) - \Im(\phi_k)\sin(\omega t)\right] e^{\xi t}. \tag{10}$$

2.4.1 Exciting the Flow Field and Sampling

The URANS simulations for both of the investigated cases did not experience transonic resonance but rather, reached a fairly steady flow condition. In order to capture the dynamics of the flow field it was necessary to disturb the flow field and collect snapshots at a fixed rate as the disturbance died out. This was done by restarting the URANS solver with an updated inlet pressure from a converged solution obtained for a lower nozzle pressure ratio. The snapshots were then collected as the flow field converged toward a new steady state. In Cases I and II the solver was restarted from $P_0/P_a = 1.28$ and $P_0/P_a = 2.04$ respectively. The results of the DMD can be sensitive to how the flow is disturbed and the objective was to excite as many modes as possible. The flow was sampled at 66,667 Hz giving a Nyquist frequency of 33,333 Hz. The DMD results for Cases I and II are based on 865 and

700 snapshots respectively. Therefore, the expected frequency resolution of the results was between approximately 100 Hz, corresponding to the slowest fully resolved cycle, to 30,0000 Hz. There is however no theoretical limitations to how low frequency DMD can capture [6]. The RANS mean flow solutions that were introduced in Section 2.3 were subtracted from the snapshots in each case. It should be noted that the mean flow solution was not the ensemble average of the snapshots as that would result in the DMD algorithm to reduce to a temporal discrete Fourier transform of the data, as Chen et al.[6] has shown.
One of the advantages of the DMD method is that it is possible to use some or all of the flow variables as an input for the algorithm. In the following analysis the primary results were obtained using pressure fluctuation p' as the input variable except for in Figure 9 where the axial momentum fluctuation, $(\rho u)'$, was used. A fluctuation, here, means the deviation of the snapshot data from the RANS reference solution.

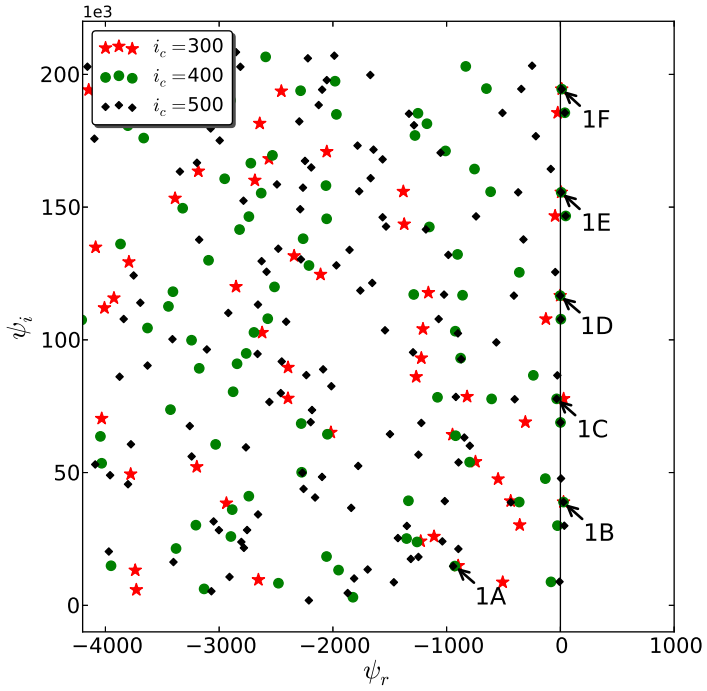

Figure 4: Case I: A logarithmic mapping of the DMD eigenvalues which separates the modes onto the unstable, right, and stable, left, complex half planes. Shown for different singular value cut off i_c = 300, 400 and 500.

3 Results

3.1 Case I

The columns of the projection base U, from the SVD, contain the orthogonal coherent structures of the flow data and each i^{th} column, also referred to as the left singular vector u_i, corresponds to a singular value σ_i such that $B^T B u_i = \sigma_i^2 u_i$. The highest singular value corresponds to the vector which accounts for the greatest variance in the data set. It is therefore logical to omit some of the singular vectors that account for the lowest variance. Figure 4 a) shows, for Case I, a logarithmic mapping of the DMD eigenvalues according to $\phi = log(\mu)/\Delta t$ which separates them onto the unstable, right, and stable, left, complex half planes. The figure shows the DMD eigenvalues using different singular vector cut off i_c, that is, using the first 300, 400 and, 500 singular vectors out of a total of 865 in Case

Table 1: Frequency and damping for the selected DMD modes of Case I.

Mode	Frequency f	damping factor ξ
1A	2355 Hz	-926.48 s^{-1}
1B	6188 Hz	-0.65 s^{-1}
1C	12377 Hz	4.89 s^{-1}
1D	18567 Hz	13.36 s^{-1}
1E	24754 Hz	1.35 s^{-1}
1F	30945 Hz	-8.54 s^{-1}

I. The figure depicts a great scatter of the eigenvalues between different cut off values. There exists, however, a number of eigenvalues that remain relatively unaffected by the cut off, which indicates that they are well resolved and reliable. These modes have been marked in the figure and selected for further analysis. Table 1 lists their respective frequencies, f, and temporal damping factor, ξ. Their frequencies have been verified by measuring the wavelengths of acoustic waves visible in the ambient flow of the modes. Looking at the table it becomes clear that Modes 1C to 1F, are the second to fifth harmonics of Mode 1B. Furthermore, Modes 1B to 1F have critically low decay/growth rates ($|\xi|$ is low). Mode 1A however, is significantly damped with a frequency corresponding roughly to one third of the frequency of Mode 1B. This is because modes 1B to 1F are odd harmonics of Mode 1A as we will see in the following analysis.

Figures 5 and 6 show the development of the pressure fluctuation, p', along the nozzle wall and centerline, respectively, over one oscillation cycle for Modes 1A and 1B. The wave profiles are computed according to Equation 10, excluding effects of damping, that is, ξ is set to zero. The values of p' are plotted 20 times, with a fixed time interval, over one oscillation cycle with the starting profile shown in red. Figure 5 a) and b), show the wall pressure fluctuations of Modes 1A and 1B respectively. They show that these modes have a similar fluctuating behavior as predicted in Ref.[1] with a standing 1/4 wave in Mode 1B and a standing 3/4 wave in Mode 1B. That is if we consider the wave form between the antinode just downstream of the shock, at $x/L \approx 0.1$, and the nozzle exit at x/L=1.0.

We further observe that the 1/4 wave has a clear node at the nozzle exit whereas the 3/4 wave has a relatively fixed node at $x/L \approx 0.4$. Moving further downstream along the 3/4 wave we see a suppression of the fluctuations near the exit rather than a fixed node. Looking at the pressure fluctuations along the nozzle centerline of Modes 1A and 1B in Figures 6 a) and b) respectively, we see that the centerline wave near the shock differs from the wall wave. The amplitude is relatively greater close to the shock, corresponding to a stronger shock at the center followed by a steep drop to negative values. These characteristics are, in principal, shared by the two modes but they differ greatly downstream of that area. Notice in particular the waves being transported downstream of the exit in Mode 1B, indicated by the crossing of the lines. This is in contrast to almost complete amplitude suppression in Mode 1A in the same region.

Figure 7 shows that Mode 1C has similar behavior as mode 1B but with half the wave length, corresponding to the doubled frequency. Notice the fixed wave node at $x/L \approx 0.7$ in Figure 7 a). Animation of the wave movement reveals that downstream of that node, the wave travels downstream and upstream of it the wave travels upstream.

Figure 8 shows the pressure fluctuation field, p', of Modes 1A to 1F. A clear pressure wave coming out of the nozzle is observed in all cases and generally they all have similar flow structures with different wave lengths depending on their frequency. This is in accordance with observations made in Figures 5 and 7.

A weak influence from the shear layer is visible in the pressure field resulting in, primarily for the higher harmonics, a slight phase shift and difference in amplitude between the jet core and shear layer. Figures 9 a) and b) show the axial momentum fluctuation field $(\rho u)'$ of modes 1A and 1B respectively. The figure shows that the influence from the velocity difference between the jet core, shear layer and, the ambient is much greater in this case as can be seen by the high phase shift between those areas.

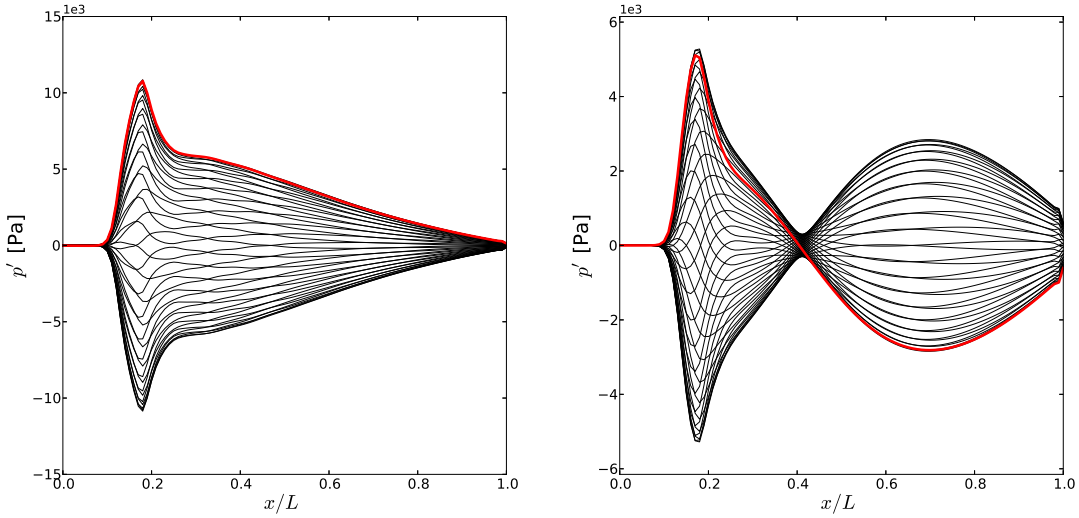

(a) Mode 1A, $f = 2355$ Hz, wall.

(b) Mode 1B, $f = 6188$ Hz, wall.

Figure 5: Case I: Development of the pressure fluctuation, p', along the nozzle wall over one oscillation cycle. The p' values are plotted 20 times at a fixed rate over one cycle with the starting values indicated by the thicker red profile. The nozzle throat and exit are located at $x/L = 0.0$ and $x/L = 1.0$ respectively.

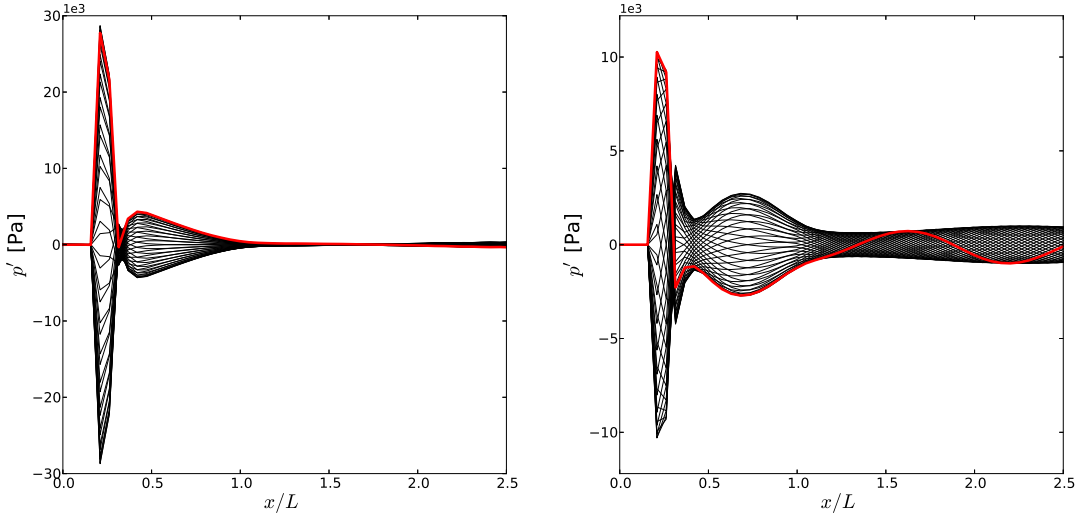

(a) Mode 1A, $f = 2355$ Hz, centerline.

(b) Mode 1B, $f = 6188$ Hz, centerline.

Figure 6: Case I: Development of the pressure fluctuation, p', along the centerline over one oscillation cycle. The p' values are plotted 20 times at a fixed rate over one cycle with the starting values indicated by the thicker red profile. The nozzle throat and exit are located at $x/L = 0.0$ and $x/L = 1.0$ respectively.

If we examine the region close to the wall, downstream of the separation, we see in Mode 1A a very thin closed region of positive fluctuation (yellow color) that extends all the way to the nozzle exit. The corresponding area in Mode 1B extends only to about half that distance. This indicates the presence of the standing 1/4 wave in Mode 1A and 3/4 wave in Mode 1B in the $(\rho u)'$ field as well.

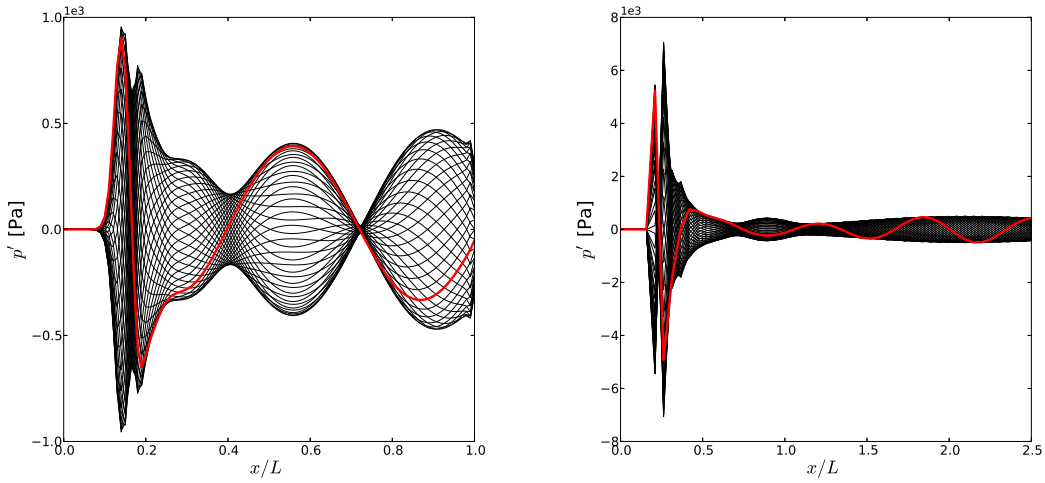

(a) Mode 1C, $f = 12377$ Hz, wall.

(b) Mode 1C, $f = 12377$ Hz, centerline.

Figure 7: Case I: Development of the pressure fluctuation, p', along the nozzle wall and centerline respectively. The p' values are plotted 20 times at a fixed rate over one oscillation cycle with the starting values indicated by the thicker red profile. The nozzle throat and exit are located at $x/L = 0.0$ and $x/L = 1.0$ respectively.

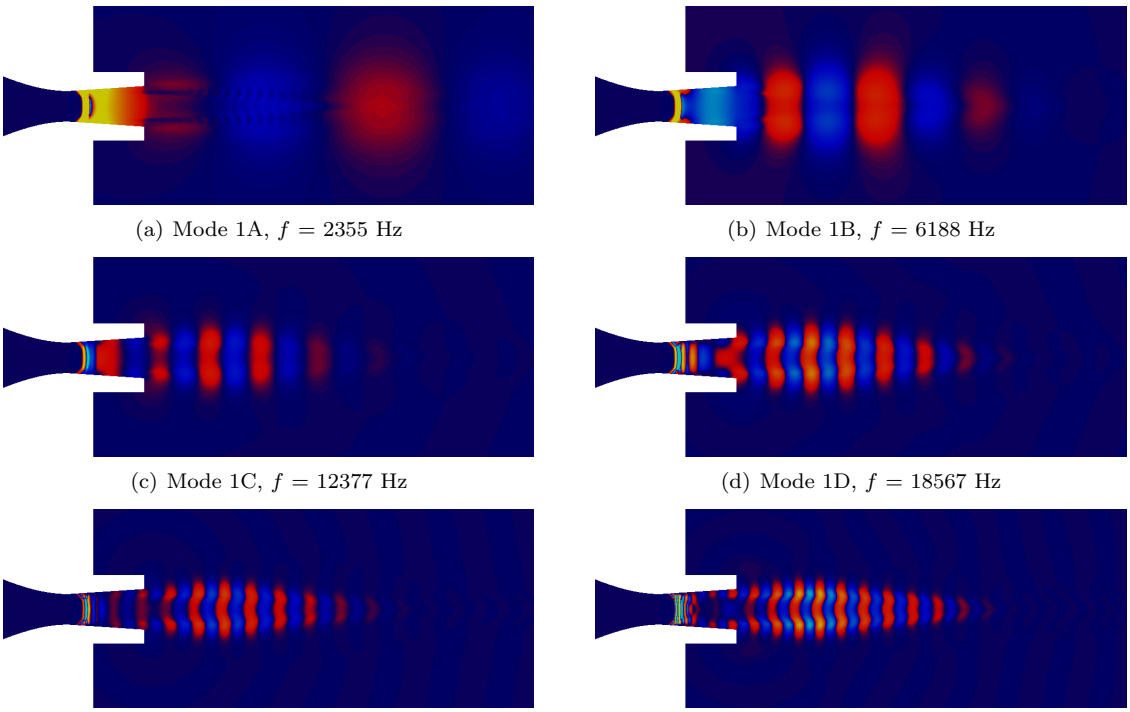

(a) Mode 1A, $f = 2355$ Hz

(b) Mode 1B, $f = 6188$ Hz

(c) Mode 1C, $f = 12377$ Hz

(d) Mode 1D, $f = 18567$ Hz

(e) Mode 1E, $f = 24754$ Hz

(f) Mode 1F, $f = 30945$ Hz

Figure 8: Pressure perturbation field, p', of selected DMD modes for Case I. Red to yellow color indicates positive pressure perturbation, yellow being highest. Dark blue to light blue indicate negative pressure perturbation, light blue being lowest.

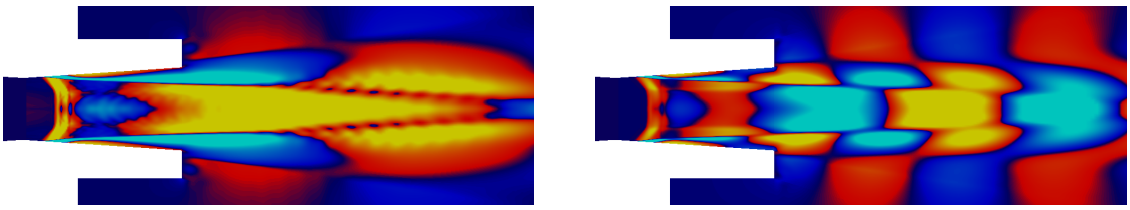

(a) Mode 1A, $f = 2355$ Hz (b) Mode 1B, $f = 6188$ Hz

Figure 9: $(\rho u)'$ perturbation field of selected DMD modes for Case I. Red to yellow color indicates positive perturbation, yellow being highest. Dark blue to light blue indicate negative perturbation, light blue being lowest.

In the experiment by Zaman et. al [1], the measured resonance frequency for nozzle pressure ratios close to that of Case I was between 6.0 and 7.0 kHz. It was concluded that the resonance for this range of pressure ratios involved a standing 3/4 wave between the shock and the nozzle exit. The current DMD analysis shows that Mode 1A, which has a standing 1/4 wave, is significantly more damped than Modes 1B to 1F. This would indicate that the flow is more prone to resonance at frequencies closer to that of Modes 1B to 1F. It is interesting to consider the norm of the modes. The modes have been normalized to fulfill Equation 7 and by computing the norm $||\mu_i^m \phi_i||$ of the i^{th} eigenmode we can see its contribution to the $(m+1)^{th}$ snapshot of the data set. Figure 10 compares the contribution of Modes 1A to 1F to the first snapshot ($m = 0$) and the 101^{st} snapshot ($m = 100$) respectively. We immediately see that Mode 1A has the greatest contribution to the first snapshot and the norms of Modes 1B to 1F decay exponentially with increasing mode frequency. The norms are plotted on a logarithmic scale and the line in the figure demonstrates how close the norms follow an exact logarithmic decay. At a later stage, $m = 100$, we see that the damping of Mode 1A has reduced its influence significantly while, because of their critically low damping or growth rates, the norms of Modes 1B to 1F remain relatively constant. This suggest that a resonance at a frequency close to the frequency of Mode 1A would be more difficult to sustain compared with a frequency close to that of Mode 1B, which has the greatest norm at the 101^{st} snapshot.

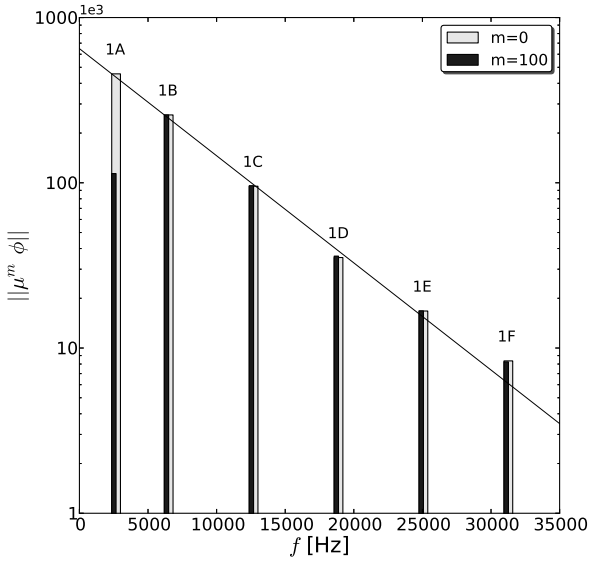

Figure 10: Case I: The norm $||\mu^m \phi||$, of Modes 1A to 1F

Table 2: Frequency and damping for the selected DMD modes of Case II.

Mode	Frequency f	damping factor ξ
2A	4854 Hz	3.88 s^{-1}
2B	9708 Hz	-1.84 s^{-1}
2C	14563 Hz	-22.39 s^{-1}
2D	19419 Hz]	-16.31 s^{-1}

3.2 Case II

Figure 11 shows the logarithmic mapping of the DMD eigenvalues for Case II. As for Case I there exists a great scatter between different cut off values. Four well resolved modes which lie on, or close to, the imaginary axis have been identified and marked in the figure. Their respective frequencies and damping factors are listed in Table 2. All of the four modes have relatively low damping/growth rates and frequencies of Modes 2B to 2D are exact harmonics of 2A's frequency.

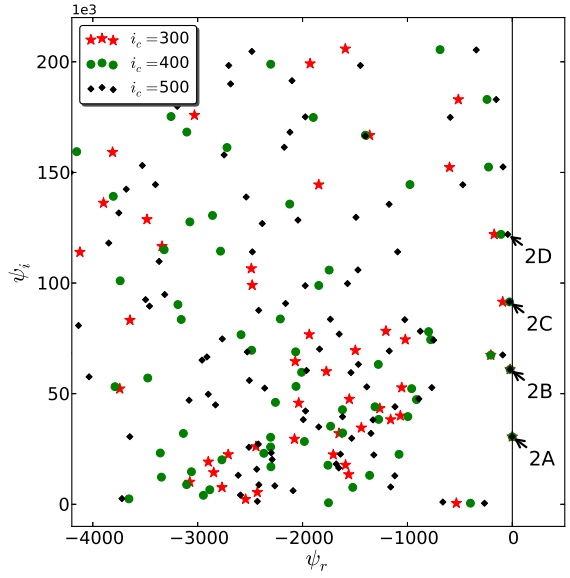

Figure 11: Case II: A logarithmic mapping of the DMD eigenvalues which separates the modes onto the unstable, right, and stable, left, complex half planes. Shown for different singular value cut off i_c = 300, 400 and 500.

The norms of Modes 2A to 2D are shown in Figure 12. They are plotted on a logarithmic scale and the line in the figure shows that the norms of Modes 2A to 2C follow an exact exponential decay. Interestingly, Mode 2D deviates from this exponential decay and is in fact more excited than Mode 2C. Notice as well the more rapid decay here compared to what was found for Case I.
Figures 13 and 14 show the development of the pressure fluctuation, p', along the nozzle wall and centerline, respectively, over one oscillation cycle for Modes 2A and 2B. These figures were realized using the same method as in Figures 5 and 6. Looking at Figure 13 a), we see that Mode 2A has a similar shape of the wall pressure fluctuation as Mode 1A. Figure 13 b) shows the wall pressure fluctuations of Mode 2B with a node at $x/L \approx 0.64$ followed by a standing, flat, antinode extending all the way to the nozzle exit.
Figure 14 a) and b) show the pressure fluctuations along the nozzle centerline of Modes 2A and 2B respectively. The vertical line in Figure 14 a) indicates a point where an upstream traveling wave

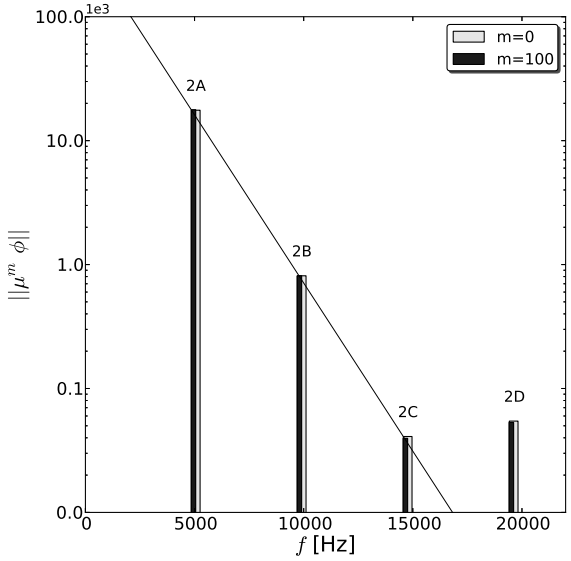

Figure 12: Case II: The norm $||\mu^m \phi||$, of Modes 2A to 2D.

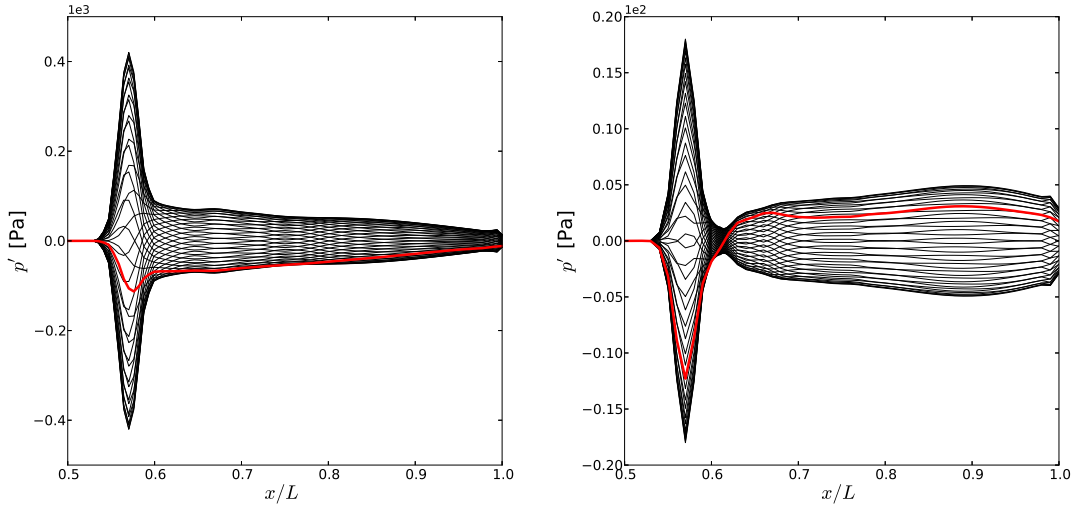

(a) Mode 2A, 4854 Hz, wall.

(b) Mode 2B, 9708 Hz, wall.

Figure 13: Case II: Development of the pressure fluctuation, p', along the nozzle wall over one oscillation cycle. The p' values are plotted 20 times at a fixed rate over one cycle with the starting values indicated by the thicker red profile. The nozzle throat and exit are located at $x/L = 0.0$ and $x/L = 1.0$ respectively.

starts to form. Notice how the wave increase in amplitude as it travels thought the shock train. An animation of the fluctuations suggests that this upstream traveling wave is superimposed on a downstream traveling wave of lower amplitude. Part of this wave can be seen downstream of the vertical line in the figure. The crossing of the wave profiles, downstream of the vertical line, shows how the wave travels downstream with relatively constant amplitude. Notice as well its greater wavelength compared to the upstream traveling wave.

Somewhat similar pattern can be seen in Figure 14 b), which shows the centerline pressure fluctuations of Mode 2B. However, animation of the fluctuations did not show a sign of superposition of two or

more waves. Rather, there seemed to be a turning point, marked with a vertical line in the figure, at which there is a standing antinode. Upstream of this point the wave travels upstream through the shock train and downstream of the point the wave travels downstream.
It is not exactly clear how the pressure wave travels upstream through the supersonic regions between the shocks. One possible explanation is that what is seen along the centerline is a component of an oblique wave moving upstream at an angle and therefore the wave component seen along the centerline moves upstream through the shocks.

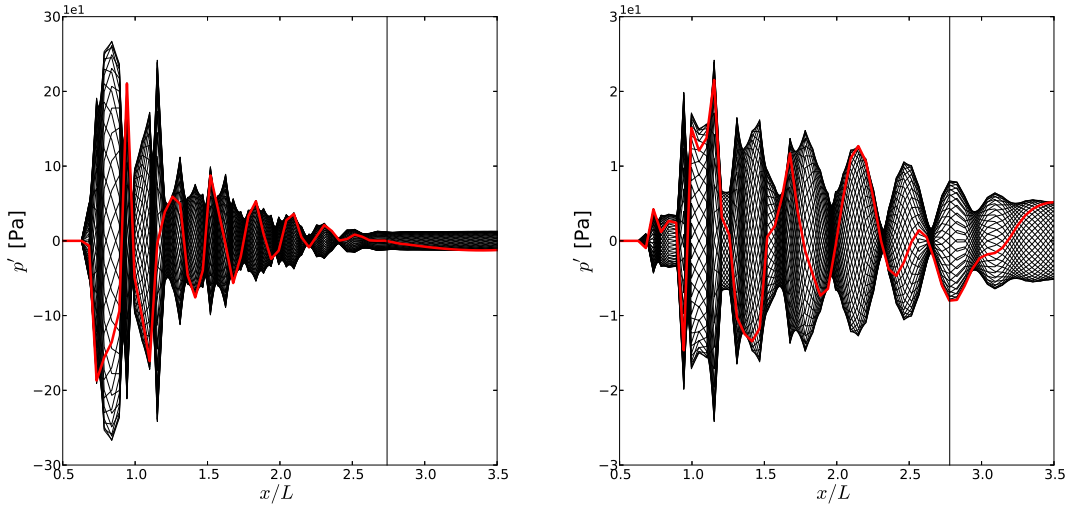

(a) Mode 2A, 4854 Hz, centerline.

(b) Mode 2B, 9708 Hz, centerline.

Figure 14: Case II: Development of the pressure fluctuation, p', along the centerline over one oscillation cycle. The p' values are plotted 20 times at a fixed rate over one cycle with the starting values indicated by the thicker red profile. The nozzle throat and exit are located at $x/L = 0.0$ and $x/L = 1.0$ respectively.

Figure 15 shows the pressure perturbation field, p', of Modes 2A to 2D. They have similar shape as the modes of Case I with a clear pressure wave coming from the shock region. The shock train is clearly visible in this case with the weaker downstream shocks having more influence on the pressure wave of the lower harmonic modes compared with the higher ones.

3.3 Comparison with Measurements

Figures 16 a) and b) compares the measured transonic tone frequencies with the primary DMD mode frequencies with respect to jet Mach number, M_j, and separation location, x_{sep}, respectively. The separation location is defined as the $x-$coordinate of the separation normalized with the length between the throat and the nozzle exit, $x_{sep} = x/L$. The experimental data are taken from Ref.[1] and are obtained for the same nozzle geometry and operating conditions as in the present study. The jet Mach number is computed according to

$$M_j = \left(\left(\frac{P_0}{P_a} \right)^{\frac{\gamma-1}{\gamma}} \left(\frac{2}{\gamma - 1} \right) \right)^{0.5}, \tag{11}$$

where P_0/P_a is the nozzle pressure ratio and γ is the specific heat ratio.

The "primary" DMD frequencies of Cases I and II are the frequencies of Modes 1B and 2A respectively. Two additional DMD analyses were performed for nozzle pressure ratios slightly lower and slightly higher than in Cases I and II respectively. The results were similar to that of Cases I and II

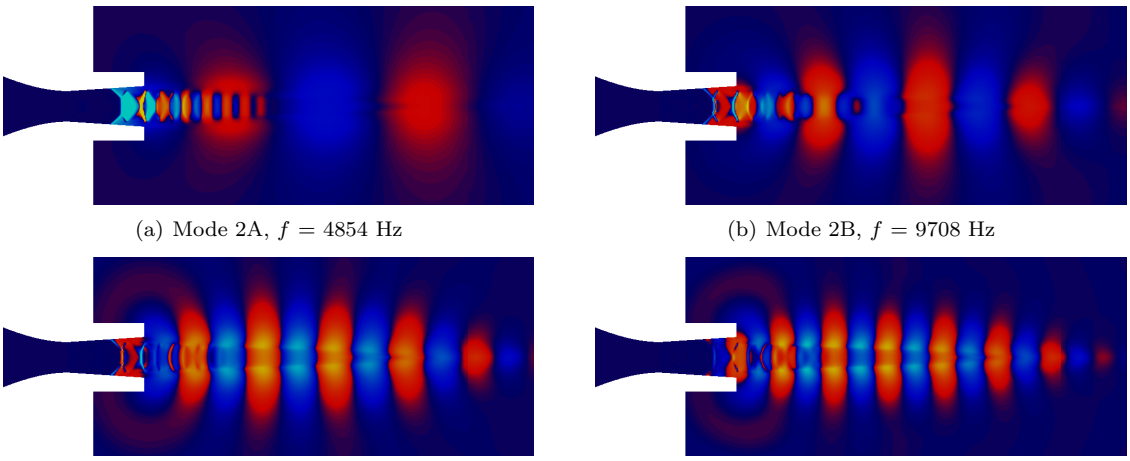

(a) Mode 2A, $f = 4854$ Hz

(b) Mode 2B, $f = 9708$ Hz

(c) Mode 2C, $f = 14563$ Hz

(d) Mode 2D, $f = 19419$ Hz

Figure 15: Pressure perturbation field, p', of selected DMD modes for Case II. Red to yellow color indicates positive pressure perturbation, yellow being highest. Dark blue to light blue indicate negative pressure perturbation, light blue being lowest.

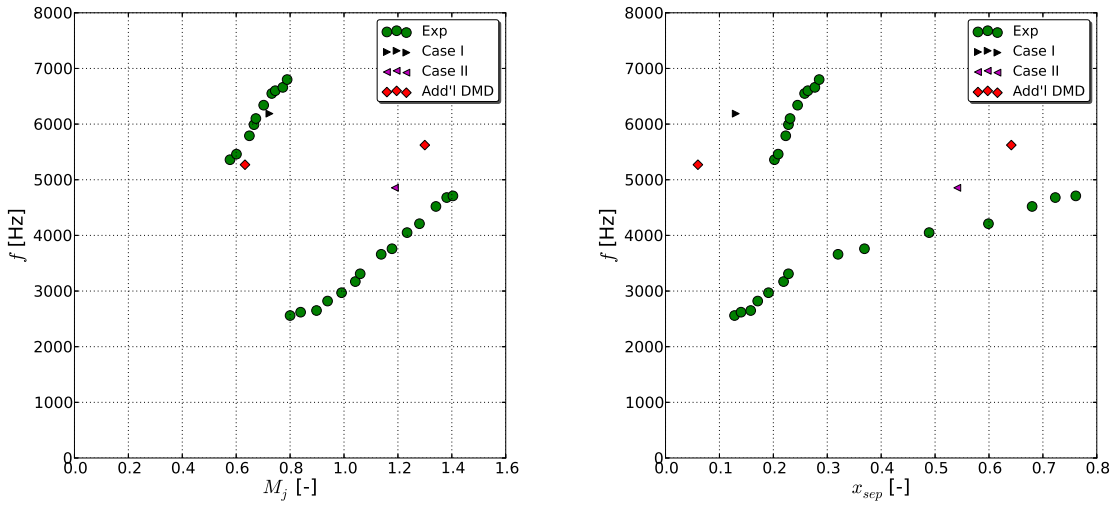

(a)

(b)

Figure 16: Experimental frequencies and DMD mode frequencies with respect to jet Mach number M_j. Experimental data are from Ref.[1].

in that they showed undamped harmonic modes with the lowest harmonic modes having the greatest norms, those being the "primary" DMD frequencies in these cases. From Figure 16 a) it is clear that the DMD frequencies for the lower jet Mach numbers are very close to those observed in the experiment. At higher jet Mach numbers the difference is greater but within the range of observed frequencies. In general, Figure 16 a) reveals that the DMD analysis captures the staging behavior observed in the experiment. However, when comparing the experimental data to the DMD data with respect to separation location x_{sep}, in Figure 16 b), the results for the lower pressure ratios do not agree. This is understandable since the RANS solution fails to predict the separation location found in the experiment, this is shown in Figure 17. A standard $k - \varepsilon$ model, or any turbulence closure of that kind for that matter, will most unlikely be able to predict the separation location very exactly.

Furthermore, as mentioned in the introductory part, the small angle of the diverging part of the nozzle makes small differences in flow conditions lead to large differences in separation location, which further hampers the prediction of the separation location.
Both experimental and numerical data show that the resonance frequency increases with decreasing distance between the shock and the nozzle exit, *within a resonance stage*. Figure 16 b) shows that the resonance frequency is not completely dominated by this distance but that the separation type, and shock pattern, which is defined by the nozzle pressure ratio and nozzle contour, determine the frequency as well.

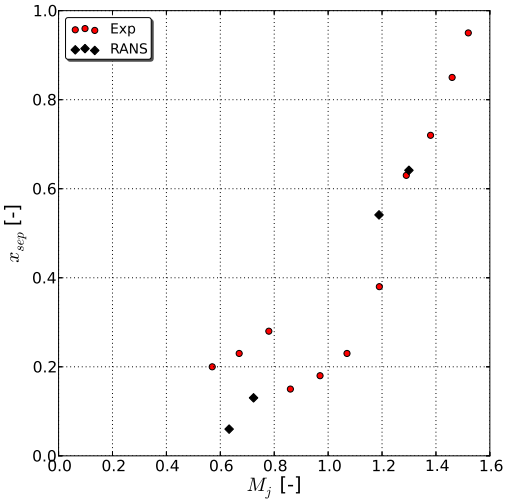

Figure 17: Separation location, $x_{sep} = x/L$, versus jet Mach number, M_j. Experimental data are from Ref.[1].

4 Summary and Conclusion

The DMD algorithm, proposed by Schmid [3], has been applied to a set of flow field snapshots from an axisymmetic URANS simulation of a separated flow inside an axisymmetric convergent-divergent nozzle. The investigated nozzle has been known to experience so called transonic resonance under off design conditions [1]. This happens when the supersonic flow separates inside the nozzle, resulting in a shock residing in the divergent part of the nozzle. The aim of the study was to investigate if the DMD analysis method described in this paper is capable of predicting the transonic resonance frequencies.
A URANS simulation of the nozzle flow did not experience transonic resonance and converged to stable solution. In order to capture the URANS flow dynamics with the DMD algorithm it was necessary to disturb the flow field.
The results show that the DMD algorithm does provide undamped, harmonic modes with frequencies close to those observed in the experiment by Zaman et al.[1]. Furthermore, the DMD modes have standing pressure waves inside the divergent part similar to what was suggested in Ref. [1]. The results further indicate a feedback loop where a pressure wave travels upstream through the jet core similar to the observations made by Olson and Lele [4].
Therefore it is concluded that the method applied in this study can predict the resonance frequencies within a reasonable range and consequently, it can shed some light on the mechanism behind the phenomena.
These results are encouraging considering how computationally cheap they were to produce compared to a full three dimensional simulations. The results also reveal that the primary mechanism responsible for the resonance is embedded in the two dimensional axisymmetric RANS equations. However, the axial symmetry of the resonance fluctuations had already been realized from the experimental data in

Ref. [1] and the axisymmetric numerical simulations in Ref. [2]. Despite that, it cannot be ignored that in a real flow, azimuthal modes could be present and interact with the axisymmetric modes. These effects are obviously not present in the current method and could be contributing to any discrepancies between the DMD results and the experiments.
Other effects, which the RANS simulations are neglecting, are worth mentioning:

Elasticity: The nozzle in this study is rigid and therefore fails to capture possible movement or deformation of the real nozzle.

Nozzle wall heat transfer: The surface of the nozzle is treated as adiabatic. However, that is unlikely to have great effect on the results here, as the flow is cold.

Wall roughness and boundary layer details: Wall roughness is not considered and the characteristics of the boundary layer are modeled using a turbulence model with wall functions. This can greatly affect the results in two ways. First, it influences the location of the separation. We saw in Figure 17 that the separation location is not well predicted for the lower jet Mach numbers and this is attributed to the low divergence angle of the nozzle and the failure to capture the dynamics of the incoming boundary layer. Secondly, this could be linked to why the URANS solver does not experience the transonic resonance. Tripping the boundary layer upstream of the nozzle throat in Ref. [1] had such an effect on the resonance tone that in some cases it was completely suppressed. It is therefore clear that the characteristics of the incoming boundary layer and the nozzle wall surface greatly affect the intensity of the resonance; although they seemed not to affect the frequency in Ref. [1].

Improving these limitations of the RANS simulations are not the aim of the present study. However, in cases of high pressure ratios, such as Case II, the shock pattern is more complex compared to the lower pressure ratio cases, such as in Case I. These complex patterns can be hard to predict accurately in a RANS simulation because of their sensitivity to numerical schemes and mesh density. A mesh sensitivity study has yet to be performed.
Now that the major limitations of the RANS solution have been discussed we finish with a short comment on the DMD modes. The fact that the DMD results provide harmonic modes shows that the resonance dynamics are nonlinear and the ability of the DMD method to capture this shows one of the advantages of not explicitly linearizing the flow dynamics. The DMD algorithm approximates the eigenmodes of a *linear* approximation of the flow dynamics in the snapshots. This means that the DMD modes are only valid for small perturbations. Let us consider an accurately predicted *growing* DMD mode. If it is excited in the nonlinear flow it will eventually develop into a limit cycle where nonlinear effects prevent it to grow further and that can possibly alter the mode frequency.

5 Acknowledgments

This work is funded by the Swedish National Space Board. Technical guidance from GKN Aerospace Sweden AB is also gratefully acknowledged.

References

[1] Zaman, K., B., M., Q., Dahl, Benicic, T. J. and Loh, C. Y., "Investigation of a 'transonic resonance' with convergent-divergent nozzles". *Journal of Fluid Mechanics*, Vol. 467, 2002, pp. 313-343

[2] Ching, Y., L., and Zaman, K., B., M., Q., "Numerical Investigation of Transonic Resonance With a Convergent-Divergent Nozzle". *AIAA Journal*, Vol. 40, No. 12, 2002, pp. 2393-2401.

[3] Schmid, P., J., "Dynamic Mode Decomposition of Numerical and Experimental Data", *Journal of Fluid Mechanics*, Vol. 656, 2010, pp. 5-28

[4] Olson, B.J. and, Lele, S.K., "A mechanism for unsteady separation in over-expanded nozzle flow",*Physics of Fluids*, Vol, 25, Issue 11, 30 August 2013, Article number 110809.

[5] Östlund, J., and Muhammad-Klingmann, B., "Supersonic Flow Separation with Application to Rocket Engine Nozzles", *Applied Mechanics Reviews*, Vol. 58, 2005, pp.143-177.

[6] Chen, K., K., Tu, J., H., and Rowley, C., W., "Variants of Dynamic Mode Decomposition: Boundary Condition, Koopman, and Fourier Analyses", *Jounal of Nonlinear Science*, Vol. 22, 2012, pp.887-915.